

UC Santa Barbara

UC Santa Barbara Previously Published Works

Title

Modeling singular mineralization processes due to fluid pressure fluctuations

Permalink

<https://escholarship.org/uc/item/39h2d2wn>

Authors

Xiong, Yihui
Zuo, Renguang
Clarke, Keith C
[et al.](#)

Publication Date

2020-03-01

DOI

10.1016/j.chemgeo.2019.119458

Peer reviewed

1 **Modeling singular mineralization processes due to fluid pressure fluctuations**

2 Yihui Xiong^{1,2}, Renguang Zuo^{1,*}, Keith C. Clarke², Stephen A. Miller³, Jian Wang⁴

3 ¹State Key Laboratory of Geological Processes and Mineral Resources, China University of Geosciences,
4 Wuhan 430074, China

5 ²Department of Geography, University of California, Santa Barbara, CA, USA 93106-4060

6 ³Center for Hydrogeology and Geothermics, University of Neuchatel, rue Emile Argand 11, Neuchâtel,
7 Switzerland

8 ⁴Key Laboratory of Geoscience Spatial Information Technology of Ministry of Land and Resources,
9 Chengdu University of Technology, Chengdu, 610059, Sichuan, China

10 *Corresponding Author. Email: zrguang@cug.edu.cn

11

12 **Abstract**

13 Mineralization in the Earth's crust can be regarded as a singular process resulting in large amounts of
14 mass accumulation and element enrichment over short time or space scales. The elemental concentrations
15 modeled by fractals and multifractals show self-similarity and scale-invariant properties. We take the view
16 that fluid-pressure variations in response to earthquakes or fault rupture are primarily responsible for
17 changes in solubility and trigger transient physical and chemical variations in ore-forming fluids that
18 enhance the mineralization process. Based on this general concept, we investigated mineral precipitation
19 processes driven by rapid fluid pressure reductions by coupling mineralization to a cellular automaton
20 model to reveal the nonlinear mechanism of the orogenic gold mineralization process using simulation. In
21 the model, fluid pressure can increase to the rock failure condition, which was set as lithostatic pressure at
22 a depth of 10km (270MPa), due to either porosity reduction or dehydration reactions. Rapid drops in
23 pressure resulting from fault rupture or local hydrofracture may induce repeated gold precipitation. The
24 geochemical patterns generated by the model evolve from depletion to enrichment patterns, and from

25 spatially random to spatially clustered structures quantified by multifractal models and geostatistics.
26 Results show how metal elements self-organize to form high metal concentration patterns displaying self-
27 similarity and scale-invariance. These transitions are attributed to the growth and coalescence of sub-
28 networks with different fluid pressures up to the percolation threshold, resulting in a wide range of fluid
29 pressure reductions and mineral precipitation in the form of clusters. The results suggest that cyclic
30 evolution of fluid pressure and its effects on gold precipitation systems can effectively mimic the repeated
31 mineralization superposition process, and generate complex geochemical patterns characterized by a
32 multifractal model. The nonlinear behavior exhibits scale-invariance and self-organized critical threshold,s
33 where mineral phase separations result from fluid pressure reductions associated with fault failure.
34 **Keywords:** Singular mineralization process; Fluid pressure fluctuation; Cellular automaton; Self-organized
35 criticality

36

37 **1. Introduction**

38 The interactions of fluid flow, seismicity, and mineral precipitation can control the mechanical
39 strength and permeability of faults in the earth's crust, and are indispensable components in the
40 development of hydrothermal systems and the formation of ore deposits (Sibson, 1987; Sibson et al., 1988;
41 Cox, 1995; Weatherley and Henley, 2013). Mechanisms responsible for generation and maintenance of high
42 fluid pressure are closely related to the spatial (Rice, 1992) and temporal (Walder and Nur, 1984)
43 variations of local permeability. In seismic zones, fluid pressure increases within impermeable zones and
44 occurs from creep compaction (Sprunt and Nur, 1977), pressure solution (Sleep and Blanpied, 1992),
45 fracture healing and sealing (Walder and Nur, 1984; Sibson et al., 1988; Blanpied et al., 1992). In addition,
46 direct fluid sources involving fluids at depth or from devolatilization reactions have also been considered
47 as mechanisms for elevated fluid pressure (Rice, 1992; Ko et al., 1995; Miller et al., 2003; Bodnar et al.,

48 2007). Once the fluid pressure increases to a level sufficient to permit frictional slip at low fault shear stress,
49 permeability instantaneously increases by several orders of magnitude to locally extremely high values
50 (Miller and Nur, 2000). The rapid fluid pressure reductions due to fault ruptures can induce boiling, or
51 phase separation of ore fluids contributing to mineral deposition (Sibson, 1987; Sibson et al., 1988;
52 Wilkinson and Johnston, 1996; Weatherley and Henley, 2013; Peterson and Mavrogenes, 2014). Rapid
53 deposition during a fluid pressure decrease seals fractures, returning permeability again to a very low
54 value, and the cycle repeats (Sibson et al., 1988; Sibson, 1992).

55 This well-known fault-valve process is widely linked to the formation of mesothermal gold mineralization
56 because the rapid fluid pressure reductions due to fault ruptures can result in anomalous enrichment of
57 elements in small ore bodies within a relatively short period of time (Sibson et al., 1988; Wilkinson and
58 Johnston, 1996; Weatherley and Henley, 2013; Peterson and Mavrogenes, 2014; Sanchez-Alfaro et al., 2016;
59 Moncada et al., 2019). This process is in accordance with the singular mineralization process, which can
60 result in anomalous amounts of mass accumulation and element enrichment within a narrow spatio-
61 temporal interval (Cheng, 2007, 2008; Zuo et al., 2009). The end products of the singular mineralization
62 processes often show complex non-linear properties, and can be modeled by fractals and multifractals
63 (Cheng et al., 1994; Cheng and Agterberg, 1996; Agterberg, 1995; Cheng et al., 2000; Cheng, 2007, 2008; Zuo
64 et al., 2009; Zuo and Wang, 2016; Zuo, 2016, 2018).

65 The concept of fractals introduced by Mandelbrot (1983) primarily represents irregular geometry by
66 its Hausdorff (or fractal) dimension, which is greater than its topological dimension. Multifractals are
67 spatially intertwined fractals with a continuous spectrum of fractal dimensions, which can be used for
68 describing complexity and self-similarity in nature. Examples include the spatial distribution of geological
69 and geochemical quantities, such as mineralization-related element concentrations in rock or related
70 surface media, such as water, soils, and stream sediments (Cheng et al., 1994; Cheng and Agterberg, 1996;
71 Cheng, 1999; Cheng, 2007). Both deterministic and stochastic physical models, such as self-organized

72 criticality, multiplicative cascade processes, diffusion limited aggregation, turbulence and Brownian
73 motion (Bak et al., 1987; Schertzer and Lovejoy, 1987; Evertsz and Mandelbrot, 1992) illustrate the
74 generation of fractals or multifractals. For example, the theory and concept of multiplicative cascade
75 processes play an important role describing intermittent turbulence and nonlinear processes (Schertzer
76 and Lovejoy, 1987). The de Wijs model (De Wijs, 1951; Agterberg, 2001) is a simple multiplicative cascade
77 model widely applied for explaining the generation mechanism of multifractal patterns and their basic
78 singularity characteristics in regional exploration geochemistry (Agterberg, 2001, 2007; Cheng, 2005; Xie
79 and Bao, 2004). However, they cannot efficiently reflect the effects of the variations in extreme physical
80 processes (e.g. fluid pressure fluctuation) on the evolution of the hydrothermal systems. As a numerical
81 equivalent of the fault valve model, the coupled cellular automaton with shear stress and fluid pressure
82 proposed by Miller et al. (1996, 1999) is expected to simulate the singular mineralization process from fluid
83 pressure fluctuation. In this model, fluid flow within a fault zone is modeled as a simple cellular
84 automaton model with a 'toggle switch' permeability assumption (Miller and Nur, 2000). That is,
85 permeability is set to two extreme states, either zero when the fluid pressure fails to reach the failure
86 conditions along the fault plane, or infinite to the nearest neighbors when the fluid pressure reaches the
87 condition, and a dilatant slip event occurs (Miller and Nur, 2000). The dynamical system between shear
88 stress and the state of the fluid pressure exhibits an evolution to a complex stress state that results in scale-
89 invariant and self-organizing behavior (Miller et al., 1996, 1999; Miller and Nur, 2000; Fitzenz and Miller,
90 2001; Miller, 2002; Miller et al., 2003).

91 However, these models focused on the dynamic interaction between earthquakes and dehydration
92 reactions, and did not address mineral precipitation processes associated with rapid fluid pressure
93 reductions. Gold solubility in hydrothermal solutions is dominantly controlled by temperature, pressure,
94 pH, and redox (e.g., Seward, 1973). A drop in pressure alone initiates gold precipitation (Loucks and
95 Mavrogenes, 1999), yet decompression also triggers phase separation where the exsolution of volatiles

96 drastically alters fluid chemistry to induce precipitation. Recent studies have suggested that precious
97 metal solubilities are strongly dependent on water vapor phase as the density of the fluid changes, which
98 is an indirect measure of changing fluid pressure (Migdisov and Williams-Jones, 2013). The abrupt
99 reductions in fluid pressure may have a dramatic effect on the aqueous solubility of quartz (Walther and
100 Helgeson, 1977) and are likely to play a major role in co-precipitation of gold with silica during each fault
101 rupture (Helgeson and Lichtner, 1987; Migdisov and Williams-Jones, 2013; Weatherley and Henley, 2013).

102 In this study, we integrated the mineral precipitation process into the fluid flow cellular automaton to
103 investigate the basic nonlinear behaviors of the orogenic gold mineralization process during rapid fluid
104 reductions due to fault failure at a depth of 10km (270MPa). We coupled gold precipitation processes to
105 the model of Miller and Nur (2000) to investigate how metal elements self-organize to form ore deposits
106 with high metal concentrations showing self-similarity. The complexity and self-similarity of generated
107 metal concentrations was further quantified by a multifractal model and geostatistics (Matheron, 1962;
108 Goovaerts, 1999).

109

110 **2. Models**

111 2.1 Numerical model

112 Cellular automata can generate very complex forms according to a simple set of local rules
113 governing interactions among nearest neighbors, and thus are attractive for the study of critical
114 phenomena and phase transitions (Wolfram, 1984; Bak et al., 1987; Bak and Tang, 1989; Miller et al., 1996).
115 We assume a grid of cells at depth representing a cross section through an active fault zone. The state of
116 each cell within a fault plane is determined by fluid pressure P_i , which is in hydraulic isolation from its
117 neighbors until a failure condition is reached. When the fluid pressure is sufficient to induce hydro-
118 fracture or other failure mechanism such as frictional sliding, the permeability is assumed infinite to the
119 nearest neighboring cells and fluid pressure equilibrates with neighboring cells by conserving fluid mass.

120 The fluid pressure in each cell within the impermeable fault zone is increased at a uniform driving rate at
 121 each time-step (t):

$$122 \quad P_f \rightarrow P_f + \frac{\partial P_f}{\partial t} \Big|_{\text{noflow}}, \quad \frac{\partial P_f}{\partial t} \Big|_{\text{noflow}} = \frac{(\dot{\Gamma} - \dot{\phi})_i}{\phi_i(\beta_\phi + \beta_f)_i} \quad (\text{Eq. 1})$$

123 where $\dot{\Gamma} - \dot{\phi}$ represents the fluid pressure source coupled with a time dependent porosity reduction ($-\dot{\phi}$)
 124 and a direct fluid source ($\dot{\Gamma}$), ϕ_i represents the initial porosity in cell i ; and β_ϕ and β_f represent the pore
 125 and fluid compressibility, respectively, often lumped into a single parameter $\beta = \beta_\phi + \beta_f$ (Segall and Rice,
 126 1995; Wong et al., 1997). Porosity reduction mechanisms (e.g., fault compaction and pressure solution) and
 127 a direct fluid source (e.g., dehydration/decarburization reactions) contribute to the increases of fluid
 128 pressure acting on discrete cells of a zero permeability fault plane. Once fluid pressure exceeds the
 129 lithostatic load, failure occurs, and the failed cells and their immediate neighboring cells are labeled. The
 130 fluid pressure instantaneously equilibrates with these hydraulically connected cells by conserving fluid
 131 mass, ignoring any gravity effect. The equilibrium fluid pressure within the affected cells updates to:

$$132 \quad \bar{P} = \frac{\sum_{i=1}^N (\phi\beta)_i P_i}{\sum_{i=1}^N (\phi\beta)_i} \quad (\text{Eq. 2})$$

133 where P_i and \bar{P} represent the pre-failure and post-failure pore pressure among the affected cells,
 134 respectively, and N is the number of affected cells. The fluid pressure redistribution might cause the
 135 neighboring cells to reach the failure condition, leading to further pressure equilibrium and cascading
 136 failure until the stress value in all the cells recovers to below the failure condition. It is important to note
 137 that the numerous mechanisms (e.g., crack porosity production due to hydro-fracture, variation of
 138 mechanical strength, and time-dependent healing), that are responsible for the evolution of fluid pressure,
 139 are simplified in this model (Miller and Nur, 2000).

140 Once the fault rupture occurs, the abrupt drop in fluid pressure toward hydrostatic values triggers
141 mineral precipitation in the fracture network, which can seal fractures to rebuild the fluid pressure and
142 ensure that the cycle repeats. The relationship between the solubility of elements and fluid pressure is
143 different for different temperature ranges. Some studies suggest that the solubility of metal ion species (e.g.
144 Ag, Au, Cu and Sn) decreases log-linearly with decreasing water vapor pressure (Migdisov et al., 1999;
145 Archibald et al., 2001, 2002; Migdisov and Williams-Jones, 2005). Other studies show an exponential
146 relationship between metal ions and water vapor pressure with the change of temperature (Bischoff et al.,
147 1986, 1988; Rempel et al., 2006; Migdisov and Williams-Jones, 2013; Migdisov et al., 2014). These studies
148 indirectly reflect that the fluid pressure can efficiently affect the solubility of precious metal solubilities.
149 We recognize that fluid pressure is not the only factor that controls metal solubility in hydrothermal
150 systems, and other physical and chemical factors, such as temperature, pH and redox, may be as
151 important or more important in some cases (Seward, 1973). Here, we ignore these other factors for the sake
152 of simplicity and focus only on the role of pressure decrease as the mechanism of metal
153 deposition. However, if the hydrothermal fluid is still undersaturated after the solubility decreases due to
154 an abrupt pressure drop, the metal will not precipitate. Thus, to simplify the model, we suppose that each
155 solubility decrease can lead to metal precipitation because the subsequent recovery stage flow of fluid
156 from the surroundings into the sealing fractures can progressively build high concentration hydrothermal
157 fluid cycle by cycle (Weatherley and Henley, 2013).

158 In this study, we used three different relationships between metal ions and fluid pressure. Specifically, we
159 investigate linear, exponential and power-law functions (Eq. 3) to estimate the volume of mineral
160 precipitation.

$$161 \left\{ \begin{array}{l} \text{Linear} : \log S_{metal} = A + B \cdot \log P_f \\ \text{Power} : \log S_{metal} = A + B \cdot (\log P_f)^C \\ \text{Exponential} : \log S_{metal} = A + B \cdot C^{\log P_f} \end{array} \right. \quad (\text{Eq. 3})$$

162 Taking the linear relationship as an example, the volume of mineral precipitation due to rapid fluid
 163 pressure reductions can be estimated by:

$$164 \quad C_{metal} = (S_{metal} - \bar{S}_{metal}) \cdot \phi\beta = 10^A \cdot (P_f^B - \bar{P}_f^B) \cdot \phi\beta \quad (\text{Eq. 4})$$

165 Here C_{metal} represents the mineral element concentration in the cells. S_{metal} and \bar{S}_{metal} represent the
 166 solubility of metals corresponding to pre-failure fluid pressure P_f and post-failure fluid pressure \bar{P}_f ,
 167 respectively, and A , B and C are constants. The cell storage capacity ($\phi\beta$) is considered as the fluid mass
 168 of each cell.

169

170 2.2 Multifractal model and singularity

171 We assume that the total concentration of deposited metal elements (e.g., Au or Ag) in the i -th cell
 172 with a linear measuring scale ε satisfies $\mu_i(\varepsilon) \propto \varepsilon^{\alpha_i}$ from a multifractal perspective, where α_i represents
 173 the singularity index. Different cells possess different singularity indices, hence the total number of cells
 174 covering the entire subset bearing the singularity α , $N_\alpha(\varepsilon)$, is proportional to $\varepsilon^{-f(\alpha)}$ ($N_\alpha(\varepsilon) \propto \varepsilon^{-f(\alpha)}$).
 175 The fractal dimension function $f(\alpha)$ is known as a multifractal spectrum, which is usually estimated via
 176 the moment method (Halsey et al., 1986). The partition function $\chi_q(\varepsilon)$ is defined as:

$$177 \quad \chi_q(\varepsilon) = \sum_{N(\varepsilon)} \mu_i^q(\varepsilon) \quad (\text{Eq. 5})$$

178 The partition function $\chi_q(\varepsilon)$ shows a power-law relationship with cell size ε for any $q \in [-\infty, +\infty]$ if the
 179 distribution of $\mu_i(\varepsilon)$ is multifractal,

$$180 \quad \chi_q(\varepsilon) \propto \varepsilon^{\tau(q)} \quad (\text{Eq. 6})$$

181 Here $\tau(q)$ represents the mass exponent of order q . The index $M = \tau(2) - 2\tau(1) + \tau(0) < 0$ suggests that the
 182 measure corresponds to a multifractal, whereas $M=0$ suggests a fractal or non-fractal.

183 The singularity exponent $\alpha(q)$ and the multifractal spectrum value can be calculated through the mass
 184 exponent by differentiation and the Legendre transformation, respectively (Evertsz and Mandelbrot, 1992)

185 $\alpha(q) = \frac{d\tau(q)}{q}$ (Eq. 7)

186 $f[\alpha(q)] = \alpha(q)q - \tau(q)$ (Eq. 8)

187 An asymmetry index $R = (\alpha(0) - \alpha_{\min}) / (\alpha_{\max} - \alpha(0))$ is defined to quantify the shape of the entire
188 multifractal spectrum (Xie and Bao, 2004; Cheng, 2014). $R > 1$ or $R < 1$ represent a left- or right-skewed
189 shape of the multifractal spectrum indicating that a local enrichment or depletion pattern dominates
190 among the whole set of cells, respectively.

191

192 2.3 Semivariogram

193 Semivariograms are a key component in geostatistics, and are typically used to quantify the degree
194 of spatial variability. The semivariogram function can be expressed as:

195 $\gamma(h) = \frac{1}{2N(h)} \sum_{i=1}^{N(h)} [Z(x_i) - Z(x_i + h)]^2$ (Eq. 9)

196 where $\gamma(h)$ represents the semivariance that quantifies the average dissimilarity between the measured
197 variable at different spatial locations. $Z(x_i)$ and $Z(x_i + h)$ represent the value of a variable at locations i
198 and $i + h$, respectively, and $N(h)$ is the number of data pairs separated by a given lag vector h . The basic
199 concepts involved in the semivariogram include a measure of the total variance (the sill, $C_0 + C$), the
200 average length of the spatial dependence (range), and the local variation due to sampling or measurement
201 error (the nugget, C_0). The degree of spatial dependence is determined by the ratio of the nugget to sill: $C_0 /$
202 $C_0 + C < 0.25$ (strong spatial dependence), $0.25 < C_0 / C_0 + C < 0.75$ (moderate spatial dependence) and $C_0 /$
203 $C_0 + C > 0.75$ (weak spatial dependence) (Cambardella et al., 1994).

204

205

206 3. Results

207 We started the simulation of fluid pressure increases and mineral precipitation process within a test
208 grid of $L \times L$ ($L = 200$) cells. Different distributions of fluid sources and material properties (simplified to
209 initial porosity and the compressibility of pore space and fluid) may determine the distribution of the fluid
210 pressure rate of increase (Miller and Nur, 2000). In our study, we considered a heterogeneous fault zone
211 where the initial value of compressibility varies, and the source term remain constant. The compressibility
212 was set between $1 \times 10^{-3} \text{ MPa}^{-1}$ and $1 \times 10^{-2} \text{ MPa}^{-1}$ based on experimental results from David et al. (1994). The
213 storage capacity was varied from $5 \times 10^{-5} \text{ MPa}^{-1}$ to $5 \times 10^{-4} \text{ MPa}^{-1}$ by setting the initial porosity to 0.05. The
214 source term was set to a constant value of $1 \times 10^{-6} \text{ yr}^{-1}$. The initial fluid pressure in each cell was distributed
215 between the hydrostatic and lithostatic pressures, in which lithostatic pressure was regarded as the failure
216 condition, and set to 270MPa corresponding to a depth of 10km. These parameters result in fluid pressure
217 increasing towards the failure condition at rates ranging from 2-20 kPa/yr. At early simulation times, cells
218 reaching failure are independent in space because the neighbors of the failed cells are far from failure, thus
219 preventing the propagation of the failure event and limiting the event size. We define event size as the
220 total number of cells reaching the failure condition during one discrete time-step. As the simulation
221 evolves, many cells approach the failure condition, and the high pressure in the failed cells can propagate
222 quickly to generate large events. Once failure occurs during the simulation, the fluid pressure in an
223 individual cell or cluster of cells experiences abrupt fluctuations from hydraulic connectivity to low
224 pressure cells. The abrupt fluid pressure drops reduce the solubility of precious metals (e.g. Ag and Au),
225 which is likely to induce co-precipitation of gold with silica during each fault rupture, and further
226 contributes to geochemical variations.

227 Similar to the evolution of high fluid pressure, the spatial distribution of metal elements evolves
228 from a spatially random structure to spatially clustered structures. Nine temporal sequence snapshots (Fig.
229 1) show the evolution and variations of geochemical patterns caused by rapid fluid pressure reductions
230 corresponding to the later time evolution. At early time steps, cells experiencing mineral precipitation are

231 randomly observed in the system due to the random failure of one or only a few cells (Figs. 1a-1d). As the
232 system evolves, more clustered spatial distributions of geochemical patterns are produced due to the
233 occurrence of mineral precipitation among a wider range of more clustered cells (Figs. 1e-1i). The ratio of
234 nugget to sill increases before the evolutionary time of 13.6 kyr and decreases after 13.6 kyr (Fig. 2),
235 indicating that the degree of spatial dependence of geochemical patterns decreases at first and then
236 increases with the further evolution of the system. This transition might be attributed to the establishment
237 of the initial structure of incipient failures and both marks the onset of a correlation length and identifies
238 the percolation threshold of the system. Around this transition point, the number of failure events,
239 cumulative event sizes and correlation length show significant fluctuations (Miller and Nur, 2000). The
240 mineral depositional process occurs in isolated failure cells that increase the spatial randomness of the
241 geochemical patterns before the transition point. When the structure of the incipient failure is established,
242 the sub-networks at different fluid pressures merge and equilibrate according to Eq. 2; thus, a wider range
243 of fluid pressure reductions results in mineral precipitation in the form of clusters, which may enhance the
244 degree of spatial dependence of geochemical patterns.

245 A transitional phenomenon also occurs with multifractal geochemical patterns. Figure 3 shows the
246 relation between the multifractal spectrum value $f(\alpha)$ and the singularity index α for different time
247 periods. The multifractal spectrum curves vary from right deviation to left deviation at approximately 13.5
248 kyr. The increasing asymmetry index (R) with the evolution of the system demonstrates that the
249 geochemical pattern evolves from a dominant local depletion pattern to local enrichment within the entire
250 matrix near the percolation threshold. Fluid pressure reductions varying from small-scale to large-scale
251 determine the scale of superimposition of metal material at different evolutionary stages. The large-scale
252 superimposition makes the components of higher value in the whole system become more pervasively
253 distributed. Thus, the enrichment of element concentrations (asymmetry indexes R in Fig. 3) rapidly

254 increases within a short period of 1.5 kyr. The index M decreases with the increase of evolutionary time,
255 indicating increasingly higher degrees of multifractality (Fig. 4).

256 Simulations end when the average fluid pressure of the system reaches the failure condition. Figure 5
257 shows the corresponding final geochemical pattern, with a high degree of spatial dependence and local
258 enrichment. The highly enriched area was found to be distributed at or near the cells with high storage
259 capacity because high storage capacity equalizes the fluid pressure to a greater extent. Therefore, more
260 dramatic fluid pressure variations occur when the cells near the high storage capacity cells fail, resulting in
261 a higher magnitude of mineral depositions. This phenomenon coincides with field observations that
262 mineral deposits or veins occur at or near the faults that determine the random and clustered features of
263 ore deposits in their spatial distributions. For example, Wang et al. (2015) revealed a clustered distribution
264 of Fe deposits in space along NNE-NE trend in Fujian Province, China. The distribution of singularity
265 index α , estimated from $\log[\mu(\varepsilon_1)/\mu(\varepsilon_2)]/\log(\varepsilon_1/\varepsilon_2)$, can quantify the properties of enrichment ($\alpha < 2$) and
266 depletion ($\alpha > 2$) of geochemical elements caused by mineral depositions (Fig. 5b).

267 Producing maps of singularities can provide new information, complementing results based on the
268 original concentration distribution (Fig. 5a) and help to recognize metal concentration anomalies from
269 complex geological regions. The multifractal spectrum of the geochemical patterns is calculated via the
270 method of moments (q), and varying from -10 to 10 in steps of 1. The corresponding parameters, partition
271 function $\chi_q(\varepsilon)$, mass exponent $\tau(q)$ and singularity exponent $\alpha(q)$, are shown in Figs. 6a-6c. The
272 multifractal spectrum obtained through a Legendre transformation (Fig. 6d) shows an asymmetric left-
273 skewed shape. This asymmetry may reflect the fact that the spatial distribution of concentrations shows a
274 continuous multifractal characteristic, which can be attributed to the periodic local mineral deposition due
275 to fluid pressure fluctuation. The results shown above are based on linear relationships between solubility
276 and fluid pressure, while Figure 7 shows the simulation results with the other two relationships (Eqs. 3b
277 and 3c). These three geochemical patterns show a similar spatial structure (Figs. 7b and 7c), and both of

278 these spatial structures are highly dependent on the distribution of the cells' storage capacity. However,
279 due to different solubility relationships, the accumulation of mineral precipitation varies, resulting in
280 different degrees of local enrichment patterns at the end of the simulation as shown by the multifractal
281 spectrum and the asymmetry index (Fig. 7d).

282

283 **4. Discussion and Conclusions**

284 We investigated the cycle of fluid pressure increase – hydrofracture – fluid pressure decrease – rapid
285 sealing from precipitation using a cellular automaton model to simulate the singular mineralization
286 process. With the continued increase of fluid pressure within the undrained system, the evolution of the
287 connectivity structure shows the onset of a correlation length at the percolation threshold, after which the
288 correlation length increases until the system as a whole reaches a critical state. The relationship between
289 cluster size and the number of events shows a power-law with an exponential tail at the percolation
290 threshold that plays an important role for fracture connectivity and fluid flow in the formation of mineral
291 deposits (Roberts et al., 1998, 1999). At the critical state, the power law statistics of cluster size indicate
292 scale invariance of the fluid pressure evolution system (cf. Fig. 6 in Miller and Nur (2000)), namely the
293 constructed cell space can occur at the level of pore structure, or at the level of large scale fluid pressure
294 within a fault zone. This determines that the distribution of elemental concentration also exhibits the scale-
295 invariance property and critical thresholds where mineral phase transitions are induced by fault failure
296 and the system seeks a new attractor (Bak et al, 1987). The scale-invariant property of geochemical patterns
297 suggests that the snapshots in Fig. 5a can be viewed as distributions of elemental concentration at a
298 microscopic scale (e.g. ore samples) or at a metallogenic zone scale. The non-uniform distribution of
299 elemental concentrations on different scales occurred in nature in mineralization systems. For example, the
300 Au concentration distribution in the Dayinggezhuang ore deposit, located in Jiaodong gold province,
301 eastern China, suggest different mineralization density at different scales (Deng et al., 2011). Self-

302 organized criticality reflects complex mineralization behavior, which is characterized by a bottom-up
303 nature where complex behavior emerges from independent but interdependent interactions of unlimited
304 cells. For example, fluid pressure in cells far from the failure condition increases independently, however,
305 fluid pressures in individual cells or many isolated networks will merge and equalize with each other after
306 the structure of incipient failure is established.

307 The interaction of physical, chemical and biological processes can contribute to mineral deposition
308 through phase transition or separation during the hydrothermal mineralization processes. We considered
309 fluid pressure fluctuations and cyclicity as a dominant process in mineralization, and this cyclicity was
310 responsible for the superposition of repeated mineralization events that ultimately produce complex
311 geochemical patterns that can be effectively modeled using a multifractal framework. Although this
312 idealized model is simple, it is not simplistic, and provides important insights into the singular
313 mineralization process. Future model developments will include other important processes not yet
314 considered, including tectonic stress increases from plate motion, to investigate how different ratios of
315 differential stress to fluid pressure can influence the fault **failure patterns which may further determine the**
316 **ore deposit types (Stephens et al., 2004).**

317

318 **Acknowledgments**

319 This research was jointly supported by the National Natural Science Foundation of China under
320 Grants 41372007 and 41522206, and MOST Special Fund from the State Key Laboratory of Geological
321 Processes and Mineral Resources, China University of Geosciences under Grant MSFGMR25.

322

323

324 **References**

- 325 Agterberg, F. P., 1995. Multifractal modeling of the sizes and grades of giant and supergiant deposits.
326 International Geology Review 37, 1-8.
- 327 Agterberg, F. P., 2001. Multifractal simulation of geochemical map patterns. In Geologic Modeling and
328 Simulation (pp. 327-346). Springer, Boston, MA.
- 329 Agterberg, F. P., 2007. New applications of the model of de Wijs in regional geochemistry. Mathematical
330 Geology 39, 1-25.
- 331 Archibald, S. M., Migdisov, A. A., Williams-Jones, A. E., 2001. The stability of Au-chloride complexes in
332 water vapor at elevated temperatures and pressures. Geochimica et Cosmochimica Acta 65, 4413-4423.
- 333 Archibald, S. M., Migdisov, A. A., Williams-Jones, A. E., 2002. An experimental study of the stability of
334 copper chloride complexes in water vapor at elevated temperatures and pressures. Geochimica et
335 Cosmochimica Acta 66, 1611-1619.
- 336 Bak, P., Tang, C., Wiesenfeld, K., 1987. Self-organized criticality: An explanation of the 1/f noise. Physical
337 review letters 59, 381-384.
- 338 Bak, P., Tang, C., 1989. Earthquakes as a self-organized critical phenomenon. Journal of Geophysical
339 Research: Solid Earth 94, 15635-15637.
- 340 Bischoff, J. L., Rosenbauer, R. J., Pitzer, K. S., 1986. The system NaCl-H₂O: Relations of vapor-liquid near
341 the critical temperature of water and of vapor-liquid-halite from 300 to 500 C. Geochimica et
342 Cosmochimica Acta 50, 1437-1444.
- 343 Bischoff, J. L., Rosenbauer, R. J., 1988. Liquid-vapor relations in the critical region of the system NaCl-H₂O
344 from 380 to 415 C: A refined determination of the critical point and two-phase boundary of seawater.
345 Geochimica et Cosmochimica Acta 52, 2121-2126.
- 346 Blanpied, M. L., Lockner, D. A., Byerlee, J. D., 1992. An earthquake mechanism based on rapid sealing of
347 faults. Nature 358, 574.

348 Bodnar, R. J., Cannatelli, C., De Vivo, B., Lima, A., Belkin, H. E., Milia, A., 2007. Quantitative model for
349 magma degassing and ground deformation (bradyseism) at Campi Flegrei, Italy: Implications for
350 future eruptions. *Geology* 35, 791-794.

351 Cambardella, C. A., Moorman, T. B., Parkin, T. B., Karlen, D. L., Novak, J. M., Turco, R. F., Konopka, A. E.,
352 1994. Field-scale variability of soil properties in central Iowa soils. *Soil science society of America*
353 *Journal* 58, 1501-1511.

354 Cheng, Q., Agterberg, F. P., Ballantyne, S. B., 1994. The separation of geochemical anomalies from
355 background by fractal methods. *Journal of Geochemical Exploration* 51, 109-130.

356 Cheng, Q., Agterberg, F. P., 1996. Multifractal modeling and spatial statistics. *Mathematical Geology* 28, 1-
357 16.

358 Cheng, Q., 1999. Multifractality and spatial statistics. *Computers & Geosciences* 25, 949-961.

359 Cheng, Q., Xu, Y., Grunsky, E., 2000. Integrated spatial and spectrum method for geochemical anomaly
360 separation. *Natural Resources Research* 9, 43-52.

361 Cheng, Q., 2005. Multifractal distribution of eigenvalues and eigenvectors from 2D multiplicative cascade
362 multifractal fields. *Mathematical Geology* 37, 915-927.

363 Cheng, Q., 2007. Mapping singularities with stream sediment geochemical data for prediction of
364 undiscovered mineral deposits in Gejiu, Yunnan Province, China. *Ore Geology Reviews* 32, 314-324.

365 Cheng, Q., 2008. Non-linear theory and power-law models for information integration and mineral
366 resources quantitative assessments. *Mathematical Geosciences* 40, 503-532.

367 Cheng, Q., 2014. Generalized binomial multiplicative cascade processes and asymmetrical multifractal
368 distributions. *Nonlinear Processes in Geophysics* 21, 477-487.

369 Cox, S. F., 1995. Faulting processes at high fluid pressures: an example of fault valve behavior from the
370 Wattle Gully Fault, Victoria, Australia. *Journal of Geophysical Research: Solid Earth* 100, 12841-12859.

371 David, C., Wong, T. F., Zhu, W., Zhang, J., 1994. Laboratory measurement of compaction-induced
372 permeability change in porous rocks: Implications for the generation and maintenance of pore
373 pressure excess in the crust. *Pure and Applied Geophysics* 143, 425-456.

374 Deng, J., Wang, Q., Wan, L., Liu, H., Yang, L., Zhang, J., 2011. A multifractal analysis of mineralization
375 characteristics of the Dayingezhuang disseminated-veinlet gold deposit in the Jiaodong gold province
376 of China. *Ore Geology Reviews* 40, 54-64.

377 De Wijs, H., 1951. Statistics of ore distribution. Part I: frequency distribution of assay values. *Journal of the*
378 *Royal Netherlands Geological and Mining Society* 13, 365-375.

379 Evertsz, C. J. G., Mandelbrot, B. B., 1992, Multifractal measures (Appendix B) [A], in Peitgen, H.-O., Jurgens,
380 H., and Saupe, D., eds., *Chaos and fractals [C]: Springer Verlag, New York*, p. 922-953.

381 Fitzenz, D. D., Miller, S. A., 2001. A forward model for earthquake generation on interacting faults
382 including tectonics, fluids, and stress transfer. *Journal of Geophysical Research: Solid Earth* 106,
383 26689-26706.

384 Goovaerts, P., 1999. Geostatistics in soil science: state-of-the-art and perspectives. *Geoderma* 89, 1-45.

385 Halsey, T. C., Jensen, M. H., Kadanoff, L. P., Procaccia, I., Shraiman, B. I., 1986. Fractal measures and their
386 singularities: The characterization of strange sets. *Physical Review A* 33, 1141.

387 Helgeson, H. C., Lichtner, P. C., 1987. Fluid flow and mineral reactions at high temperatures and pressures.
388 *Journal of the Geological Society* 144, 313-326.

389 Ko, S. C., Olgaard, D. L., Briegel, U., 1995. The transition from weakening to strengthening in dehydrating
390 gypsum: Evolution of excess pore pressures. *Geophysical Research Letters* 22, 1009-1012.

391 Loucks, R. R., Mavrogenes, J. A., 1999. Gold solubility in supercritical hydrothermal brines measured in
392 synthetic fluid inclusions. *Science* 284, 2159-2163.

393 Mandelbrot, B. B., 1983. *The fractal geometry of nature* (Vol. 173, p. 51). New York: WH freeman.

394 Matheron, G., 1962. *Traité de géostatistique appliquée*. 1 (1962) (Vol. 1). Editions Technip.

395 Migdisov, A. A., Williams-Jones, A. E., Suleimenov, O. M., 1999. Solubility of chlorargyrite (AgCl) in water
396 vapor at elevated temperatures and pressures. *Geochimica et Cosmochimica Acta* 63, 3817-3827.

397 Migdisov, A. A., Williams-Jones, A. E., 2005. An experimental study of cassiterite solubility in HCl-bearing
398 water vapour at temperatures up to 350 C. Implications for tin ore formation. *Chemical geology* 217,
399 29-40.

400 Migdisov, A. A., Williams-Jones, A. E., 2013. A predictive model for metal transport of silver chloride by
401 aqueous vapor in ore-forming magmatic-hydrothermal systems. *Geochimica et Cosmochimica Acta*
402 104, 123-135.

403 Migdisov, A. A., Bychkov, A. Y., Williams-Jones, A. E., Van Hinsberg, V. J., 2014. A predictive model for
404 the transport of copper by HCl-bearing water vapour in ore-forming magmatic-hydrothermal systems:
405 Implications for copper porphyry ore formation. *Geochimica et Cosmochimica Acta* 129, 33-53.

406 Miller, S. A., Nur, A., Olgaard, D. L., 1996. Earthquakes as a coupled shear stress-high pore pressure
407 dynamical system. *Geophysical Research Letters* 23, 197-200.

408 Miller, S. A., Ben - Zion, Y., Burg, J. P., 1999. A three - dimensional fluid - controlled earthquake model:
409 Behavior and implications. *Journal of Geophysical Research: Solid Earth* 104, 10621-10638.

410 Miller, S. A., Nur, A., 2000. Permeability as a toggle switch in fluid-controlled crustal processes. *Earth and*
411 *Planetary Science Letters* 183, 133-146.

412 Miller, S. A., 2002. Properties of large ruptures and the dynamical influence of fluids on earthquakes and
413 faulting. *Journal of Geophysical Research: Solid Earth* 107.

414 Miller, S. A., Van Der Zee, W., Olgaard, D. L., Connolly, J. A. D., 2003. A fluid-pressure feedback model of
415 dehydration reactions: experiments, modelling, and application to subduction zones. *Tectonophysics*
416 370, 241-251.

417 Moncada, D., Rimstidt, J. D., Bodnar, R. J., 2019. How to form a giant epithermal precious metal deposit:
418 Relationships between fluid flow rate, metal concentration of ore-forming fluids, duration of the ore-
419 forming process, and ore grade and tonnage. *Ore Geology Reviews* 113, 103066.

420 Peterson, E. C., Mavrogenes, J. A., 2014. Linking high-grade gold mineralization to earthquake-induced
421 fault-valve processes in the Porgera gold deposit, Papua New Guinea. *Geology* 42, 383-386.

422 Rempel, K. U., Migdisov, A. A., & Williams-Jones, A. E., 2006. The solubility and speciation of
423 molybdenum in water vapour at elevated temperatures and pressures: Implications for ore genesis.
424 *Geochimica et Cosmochimica Acta* 70, 687-696.

425 Rice, J. R., 1992. Fault stress states, pore pressure distributions, and the weakness of the San Andreas fault.
426 In *International geophysics* 51, 475-503.

427 Roberts, S., Sanderson, D. J., Gumiel, P., 1998. Fractal analysis of Sn-W mineralization from central Iberia;
428 insights into the role of fracture connectivity in the formation of an ore deposit. *Economic Geology* 93,
429 360-365.

430 Roberts, S., Sanderson, D. J., Gumiel, P., 1999. Fractal analysis and percolation properties of veins.
431 Geological Society, London, Special Publications 155, 7-16.

432 Sanchez-Alfaro, P., Reich, M., Driesner, T., Cembrano, J., Arancibia, G., Pérez-Flores, P., Heinrich, C.A.,
433 Rowland, J., Tardani, D., Lange, D., Campos, E., 2016. The optimal windows for seismically-enhanced
434 gold precipitation in the epithermal environment. *Ore Geology Reviews* 79, 463-473.

435 Schertzer, D., Lovejoy, S., 1987. Physical modeling and analysis of rain and clouds by anisotropic scaling
436 multiplicative processes. *Journal of Geophysical Research: Atmospheres* 92, 9693-9714.

437 Segall, P., Rice, J. R., 1995. Dilatancy, compaction, and slip instability of a fluid - infiltrated fault. *Journal of*
438 *Geophysical Research: Solid Earth* 100, 22155-22171.

439 Seward, T. M., 1973. Thio complexes of gold and the transport of gold in hydrothermal ore solutions.
440 *Geochimica et Cosmochimica Acta* 37, 379-399.

441 Sibson, R. H., 1987. Earthquake rupturing as a mineralizing agent in hydrothermal systems. *Geology* 15(8),
442 701-704.

443 Sibson, R. H., Robert, F., Poulsen, K. H., 1988. High-angle reverse faults, fluid-pressure cycling, and
444 mesothermal gold-quartz deposits. *Geology* 16, 551-555.

445 Sibson, R. H., 1992. Implications of fault-valve behaviour for rupture nucleation and recurrence.
446 *Tectonophysics* 211, 283-293.

447 Sleep, N. H., Blanpied, M. L., 1992. Creep, compaction and the weak rheology of major faults. *Nature* 359,
448 687.

449 Sprunt, E. S., Nur, A., 1977. Destruction of porosity through pressure solution. *Geophysics* 42, 726-741.

450 Stephens, J. R., Mair, J. L., Oliver, N. H., Hart, C. J., Baker, T., 2004. Structural and mechanical controls on
451 intrusion-related deposits of the Tombstone Gold Belt, Yukon, Canada, with comparisons to other
452 vein-hosted ore-deposit types. *Journal of Structural Geology* 26, 1025-1041.

453 Wang, Z., Zuo, R., Zhang, Z., 2015. Spatial analysis of Fe deposits in Fujian Province, China: Implications
454 for mineral exploration. *Journal of Earth Science* 26, 813-820.

455 Walder, J., Nur, A., 1984. Porosity reduction and crustal pore pressure development. *Journal of*
456 *Geophysical Research: Solid Earth* 89, 11539-11548.

457 Walther, J. V., Helgeson, H. C., 1977. Calculation of the thermodynamic properties of aqueous silica and
458 the solubility of quartz and its polymorphs at high pressures and temperatures. *American Journal of*
459 *Science* 277, 1315-1351.

460 Weatherley, D. K., Henley, R. W., 2013. Flash vaporization during earthquakes evidenced by gold deposits.
461 *Nature Geoscience* 6, 294-298.

462 Wilkinson, J. J., Johnston, J. D., 1996. Pressure fluctuations, phase separation, and gold precipitation during
463 seismic fracture propagation. *Geology* 24, 395-398.

464 Wolfram, S., 1984. Cellular automata as models of complexity. *Nature* 311, 419-424.

465 Wong, T. F., Ko, S. C., Olgaard, D. L., 1997. Generation and maintenance of pore pressure excess in a
466 dehydrating system 2. Theoretical analysis. *Journal of Geophysical Research: Solid Earth* 102, 841-852.

467 Xie, S., Bao, Z., 2004. Fractal and multifractal properties of geochemical fields. *Mathematical Geology* 36,
468 847-864.

469 Zuo, R., Cheng, Q., Agterberg, F. P., Xia, Q., 2009. Application of singularity mapping technique to identify
470 local anomalies using stream sediment geochemical data, a case study from Gangdese, Tibet, western
471 China. *Journal of Geochemical Exploration* 101, 225-235.

472 Zuo, R., Wang, J., 2016. Fractal/multifractal modeling of geochemical data: A review. *Journal of*
473 *Geochemical Exploration* 164, 33-41.

474 Zuo, R., 2016. A nonlinear controlling function of geological features on magmatic-hydrothermal
475 mineralization. *Scientific Reports* 6, 27127.

476 Zuo, R., 2018. A fractal measure of mass transfer in fluid–rock interaction. *Ore Geology Reviews* 95, 569–
477 574.

478

479

480

481

482

483

484

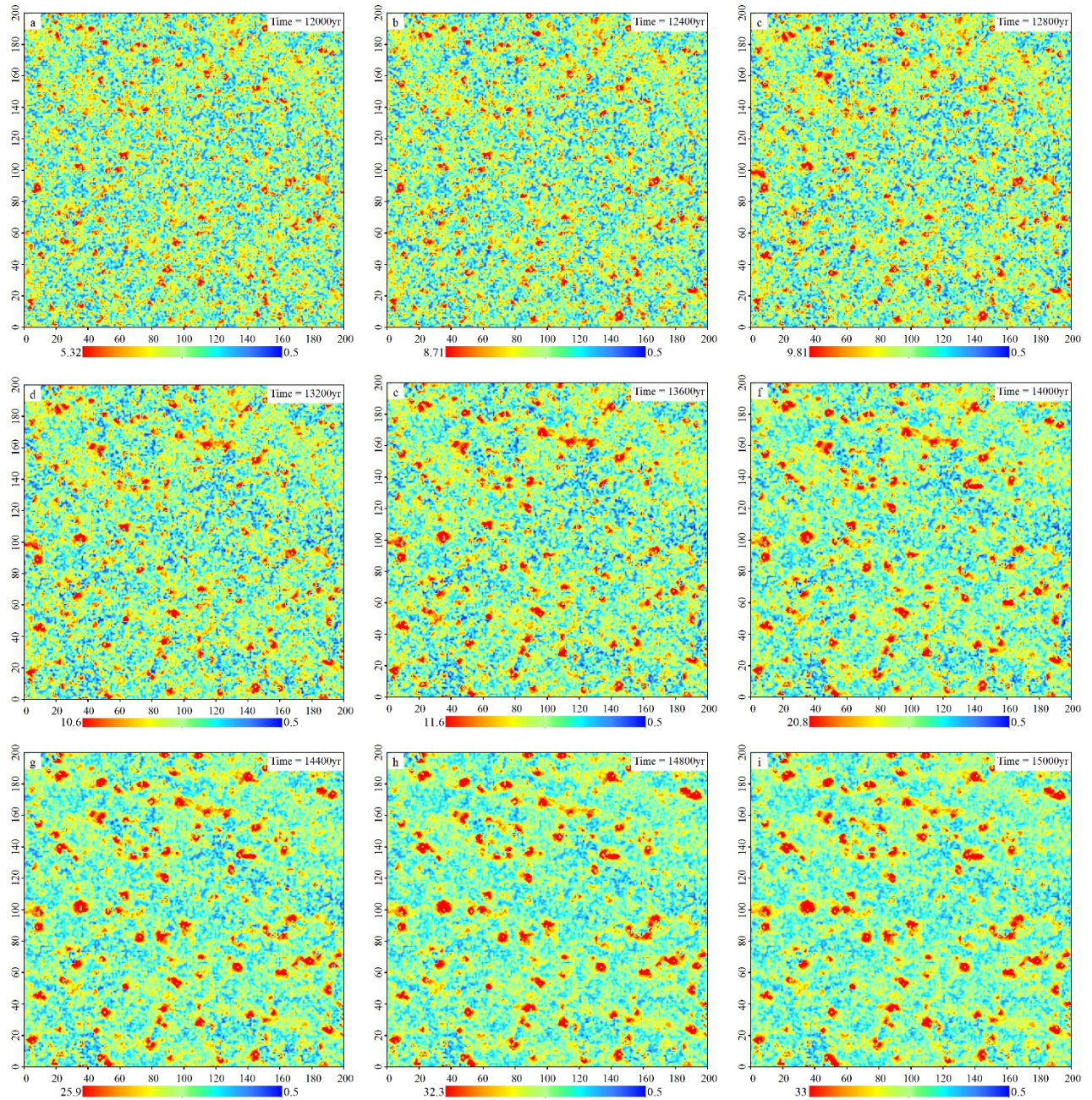
485

486

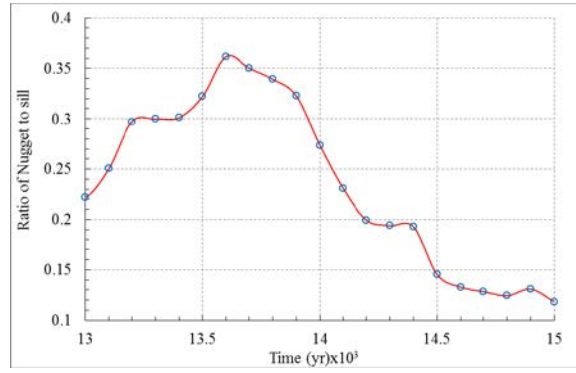
487

488

489



490 Figure 1. Nine temporal sequence snapshots showing the evolution and variations of geochemical patterns
 491 caused by rapid fluid pressure reductions corresponding to time of evolution; At early times, from (a) to
 492 (d), cells with mineral deposition randomly occur in the system due to the random failure of one or only a
 493 few cells. As the system evolves, from (e) to (i), structured spatial distributions of geochemical patterns are
 494 produced due to the occurrence of mineral deposition among a wider range of clustered cells.

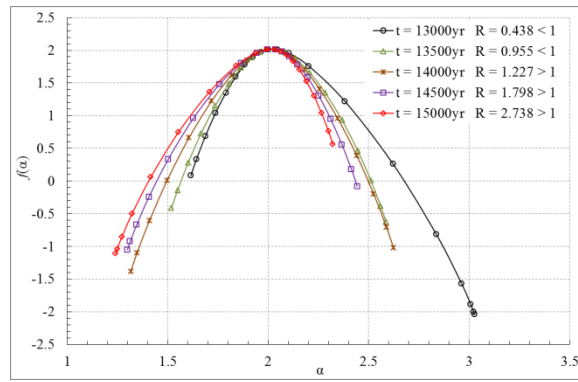


495

496

Figure 2. Time line of ratio of nugget to sill obtained from the semivariogram function.

497

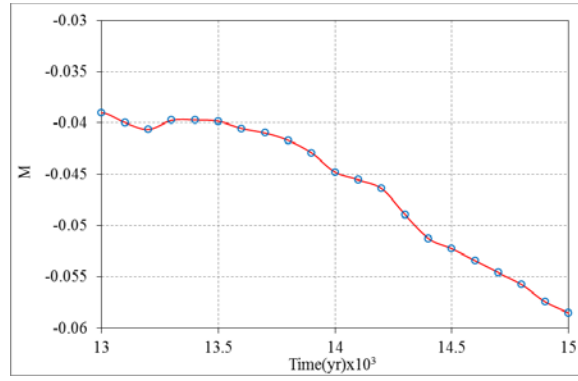


498

499

Figure 3. Multifractal spectra of geochemical patterns at different evolution times.

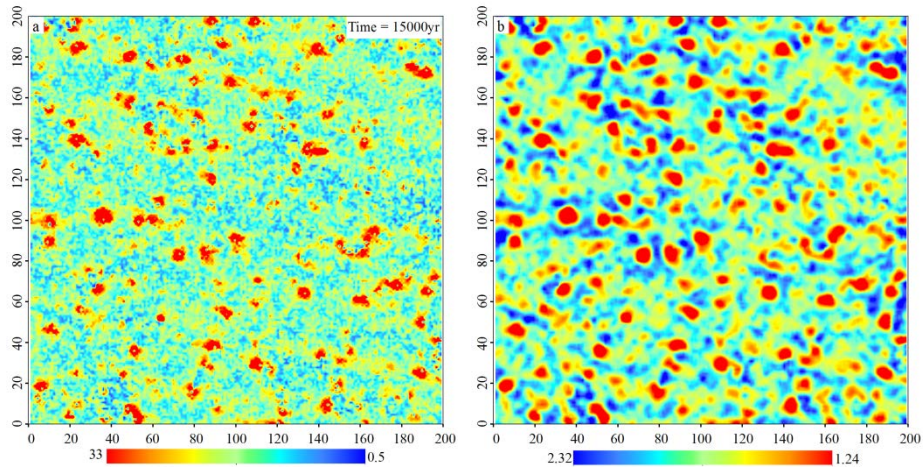
500



501

502 Figure 4. Time line of multifractality measuring the irregularity of geochemical spatial dispersion patterns.

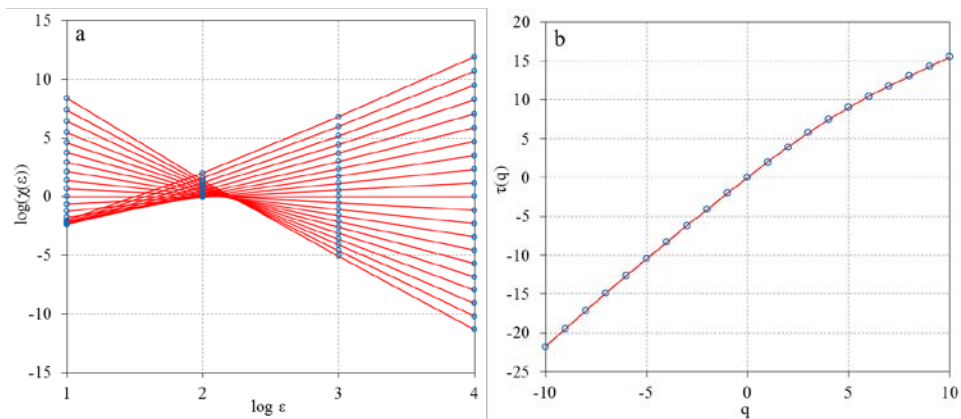
503



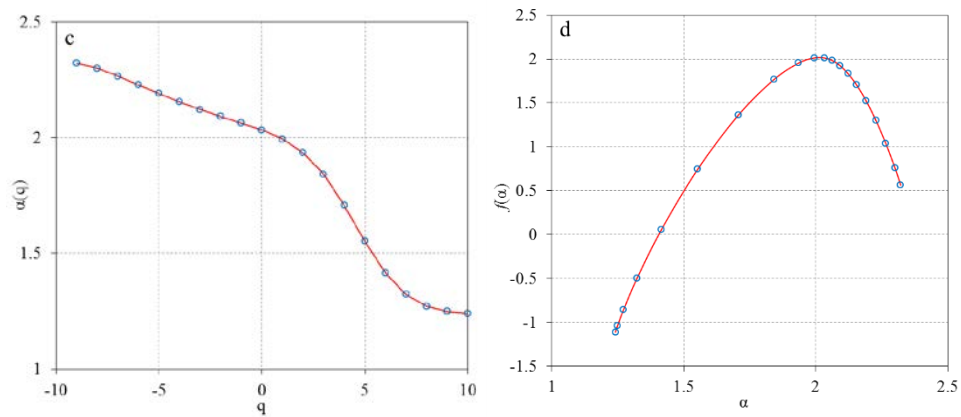
504

505 Figure 5. (a) Spatial distribution of element concentration based on linear relationships between solubility
506 and pressure; (b) Spatial distribution of singularity index α quantifying the properties of local enrichment
507 and depletion of geochemical patterns.

508

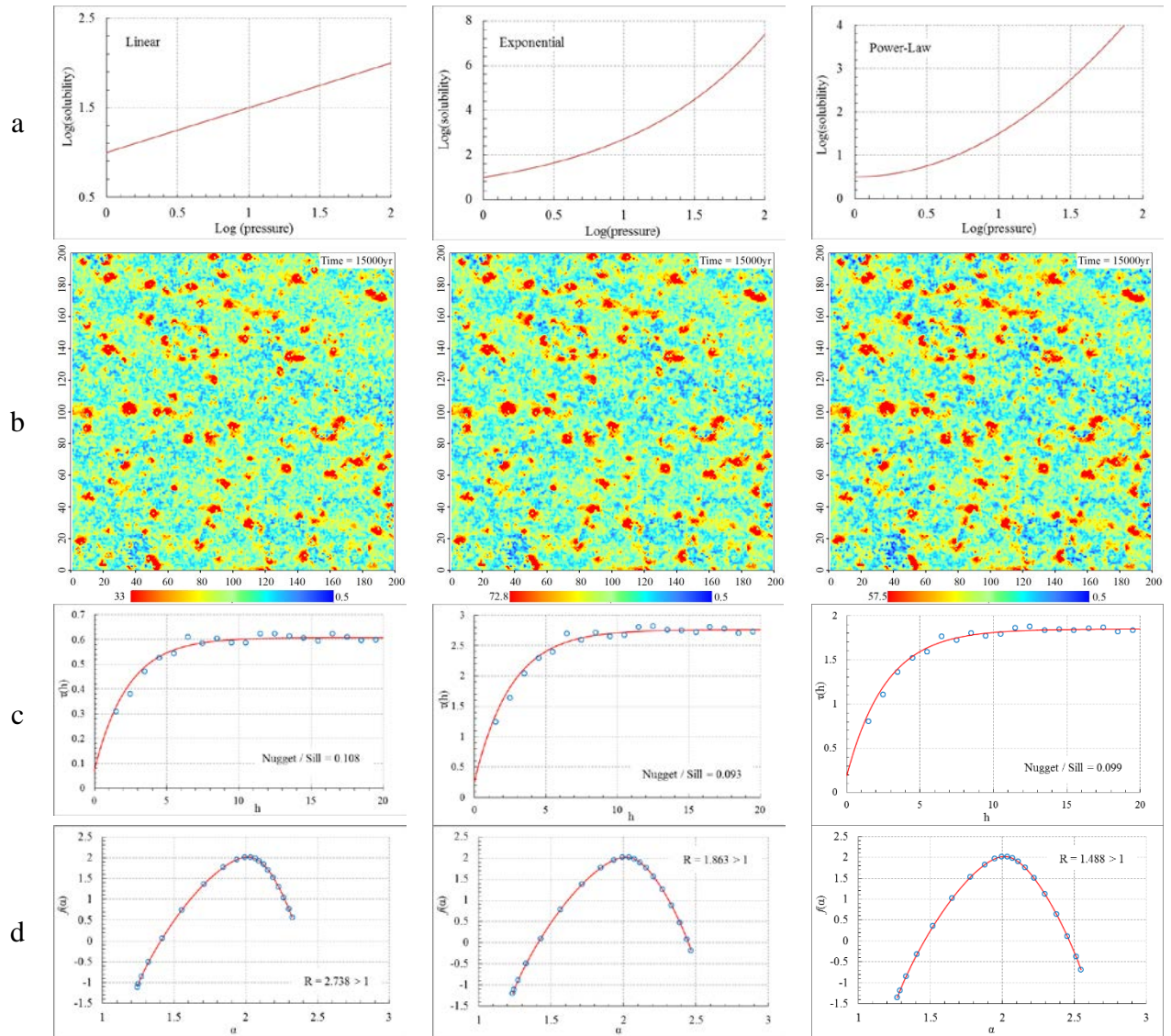


510



511

512 Figure 6. Results of multifractal analysis applied to geochemical pattern of Figure 5(a); (a) Log-log plot of
 513 mass-partition function vs. edge size of cell, model parameter q varies from -10 to 10 with 1 interval; (b)
 514 Estimates of mass exponent $\tau(q)$ involve slopes of the straight-lines in (a) vs. order q ; (c) Singularity index
 515 $\alpha(q)$ and order q ; (d) Multifractal spectra value $f(\alpha)$ vs singularity index α .



516

517 Figure 7. Row (a) Three different relationships (linear, exponential and power law) between solubility and
 518 pressure in logarithmic coordinates; Row (b) Spatial distribution of element concentration based on three
 519 different relationships based on Row (a); Row (c) and Row (d) are semivariograms and multifractal
 520 spectrums corresponding to geochemical patterns in Row (b).